



# Photocatalytic activity of N-doped and N–F co-doped TiO<sub>2</sub> and reduction of chromium(VI) in aqueous solution: An EPR study

A.E. Giannakas, E. Seristatidou, Y. Deligiannakis, I. Konstantinou \*

Department of Environmental and Natural Resources Management, University of Western Greece, G. Seferi 2, Agrinio 30100, Greece

## ARTICLE INFO

### Article history:

Received 20 July 2012

Received in revised form

10 December 2012

Accepted 13 December 2012

Available online 21 December 2012

### Keywords:

Photocatalysis

N-doped TiO<sub>2</sub>

N–F co-doped TiO<sub>2</sub>

Cr(VI) reduction

EPR

N<sub>b</sub><sup>•</sup> species

Microwave saturation

## ABSTRACT

N-doped and N–F co-doped TiO<sub>2</sub> catalysts were prepared via a sol–gel method using NH<sub>4</sub>Cl and NH<sub>4</sub>F as N and N–F dopant precursors, respectively, having Ti:N and/or F molar ratios of 1:1, 1:2 and 1:3. The catalysts were tested for the photocatalytic reduction of Cr(VI) in the presence of oxalate ions. XRD analysis showed the formation of TiO<sub>2</sub> anatase phase in all cases. UV–vis DRS spectra showed that both N–F and N-doping resulted in a decrease in the band gap energy ( $E_g$ ), at the values of 2.81 eV and 3.01 eV, respectively. Thus, N–F doped TiO<sub>2</sub> showed enhanced absorption at visible wavelengths. The structure and photodynamics of the TiO<sub>2</sub> catalysts was investigated in detail by electron paramagnetic resonance (EPR) spectroscopy. The EPR data showed that: [i] NO centers, N<sub>b</sub><sup>•</sup> and O<sub>2</sub><sup>–•</sup> radicals were formed. In addition, lattice Ti<sup>3+</sup> ions were detected in N–F co-doped solids; [ii] the N<sub>b</sub><sup>•</sup> and Ti<sup>3+</sup> species were photoactive, while the NO species were non-photoactive.

The photocatalytic efficiency for Cr(VI) reduction in the presence of oxalate ions, followed the trend TNF1 > TN1 > TNF2 > TN3 > TN2 > TNF3. Importantly, an apparent correlation between the catalytic efficiency and the concentration of N<sub>b</sub><sup>•</sup> species was revealed by EPR. The location of N<sub>b</sub><sup>•</sup> in the crystal lattice of TiO<sub>2</sub> has been assessed also by measuring their microwave saturation parameters  $P_{1/2}$ . Electron capturing by O<sub>2</sub> and subsequent generation of O<sub>2</sub><sup>–•</sup> was favored for N-doped catalysts. In contrast, in N–F co-doped catalysts, O<sub>2</sub> could not compete efficiently with Cr(VI) for the photogenerated electrons in energy states below the conduction band of TiO<sub>2</sub>, resulting in higher reduction efficiency for these catalysts.

© 2012 Elsevier B.V. All rights reserved.

## 1. Introduction

In recent years, catalytic techniques have been applied in various fields in order to solve the increasing environmental pollution [1]. Photocatalysis is a promising method that has a great potential for the conversion of solar photon energy into chemical energy and for the decomposition of pollutants in air and water [2]. Titanium dioxide (TiO<sub>2</sub>) has been widely studied and used as a photocatalyst by virtue of its low cost, chemical stability, non-toxicity and favorable optoelectronic properties. However, a serious disadvantage of TiO<sub>2</sub> as a wide band gap semiconductor ( $E_g = 3.4$  eV for anatase) is that absorbs only UV light ( $\lambda \leq 387$  nm), which accounts for only a small fraction (3–5%) of solar energy.

In order to improve the photocatalytic activity of TiO<sub>2</sub> under visible-light irradiation, many attempts have been made, including doping of TiO<sub>2</sub> with transition metals (Fe, Ce, La, etc.) [3–6]. However, metal doping has several drawbacks i.e. the doped materials present low thermal stability, while metal leaching and possible

toxicity effects diminish the applicability potential for water-treatment applications. Furthermore, in many cases, the metal centers can act as deep electron-traps, reducing the photocatalytic efficiency [7]. Another approach to narrow the semiconductor's band-gap is the replacement of lattice oxygen by anionic dopant species, such as N [7], C [8], S [9], I [10], F [11] or with co-doping such as N–I [12], N–S [13] and N–F [14]. In this way, the absorption edge of TiO<sub>2</sub> could be shifted to higher wavelengths, i.e. the doped TiO<sub>2</sub> can achieve significant photocatalytic activity under visible light irradiation [14–16].

Recent experimental studies have reported a remarkable photocatalytic activity of nitrogen and fluorine co-doped TiO<sub>2</sub> under visible light [15,16]. N-doping resulted in improvement of visible light absorption, as well as in the creation of photoinduced surface oxygen vacancies [17,18]. F-doping produced several beneficial effects such as the creation of surface oxygen vacancies, enhancement of surface acidity and formation of Ti<sup>3+</sup> centers, i.e. conduction-band electrons e<sup>–</sup><sub>CB</sub> [19]. Wang et al. [20], reported the unusual role of F in tailoring the band structure of the N-doped TiO<sub>2</sub>. By theoretical calculations and experiments, they demonstrated that incorporating F into N-doped TiO<sub>2</sub> enhances the oxidative power of the photoinduced holes in the

\* Corresponding author. Tel.: +30 26410 74186; fax: +30 26410 74176.

E-mail address: [ikonst@cc.uoi.gr](mailto:ikonst@cc.uoi.gr) (I. Konstantinou).

valence-band ( $h^+_{VB}$ ) but lessens the reduction ability of  $e^-_{CB}$ . This provides important opportunities to control the photocatalytic reactions initiated by the  $e^-_{CB}$  and  $h^+_{VB}$  pairs. Such materials could be used for the catalytic reduction of toxic metal ions such as Cr(VI). The heterogeneous photocatalytic reduction of metal ions using semiconductors has been proposed as an effective and simple method of treatment [1,20]. In the literature, the photocatalytic efficiency of N, N-F TiO<sub>2</sub> materials has been usually studied toward oxidation of organic compounds such as dyes, microcystins, and chlorophenols [7,14,22,16,23,24] while information on the reduction efficiency toward metal cations is scarce [20].

Electron paramagnetic resonance (EPR) spectroscopy has become a key-method for the characterization of N-doped and N-F co-doped TiO<sub>2</sub> materials [21,22]. EPR can provide direct information on the type, concentration and dynamics of photoinduced holes ( $h^+$ ) and electrons ( $e^-$ ) in such semiconductors. Moreover, the N-F co-doped TiO<sub>2</sub> bears N-based paramagnetic species such as  $N_b\bullet$ , NO and NO<sub>2</sub> species, which are the products of the complex oxidation process taking place during the preparation of the samples [21,22]. The EPR characteristics of these NO and  $N_b\bullet$  species have been thoroughly reviewed by Giamello et al. [22].

The present work provides novel data on the role of the N-based radical species in the photocatalytic reduction efficiency of N-doped and N-F co-doped TiO<sub>2</sub> using Cr(VI) as probe pollutant. Specific aims of the present work were: [i] to prepare N-doped and N-F co-doped TiO<sub>2</sub> catalysts with a sol-gel impregnation method; [ii] to study their photocatalytic performance for Cr(VI) reduction in the presence of oxalate ions. Oxalate was used as hole scavenger, inhibiting the recombination rate of photo-induced hole-electron pairs, thus increasing the reduction ability of the prepared catalyst. In addition, oxalate may be present in a great variety of surface waters and industrial waste effluents, therefore simultaneous treatment of Cr(VI)/oxalate may provide technological advantages, in practical applications of photocatalytic treatment; [iii] to perform a detailed in situ characterization of the various photoinduced active centers and the nitrogen paramagnetic species, formed in the N-doped and N-F co-doped TiO<sub>2</sub> solids by EPR spectroscopy. Finally, the [Cr(V)-oxalate] complexes which are involved as intermediates in the photocatalytic Cr(VI) reduction, have also been studied by EPR.

## 2. Experimental

### 2.1. Preparation of photocatalysts

The preparation of the photocatalysts was based on a simple sol-gel impregnation method [20]. N-F co-doped materials were prepared as follows: 3.4 mL titanium(IV) n-butoxide was added drop wise to 50 mL aqueous NH<sub>4</sub>F solution of different concentrations under vigorous stirring in order to obtain final [Ti:N/F] molar ratios of 1:1, 1:2 and 1:3, respectively. The so obtained milky suspension was aged for 24 h at room temperature (25 °C) and subsequently dried at 100 °C for at least 48 h. The obtained xerogels were calcined at 500 °C for 1 h in air with a ramp rate of 5 °C/min. Then, the calcined powders were dispersed in water and the suspensions were sonicated for 2 h, filtered and the powders were washed with ultrapure water to remove impurities. Finally, the as-prepared catalysts were dried again at 110 °C and ground in agate mortar. N-doped TiO<sub>2</sub> were also prepared by using NH<sub>4</sub>Cl as dopant precursor, using a similar procedure. The final solids obtained after calcination were washed several times with ultrapure water in order to remove impurities such as chloride ions until no sediment (AgCl) or turbid solution was formed with the addition of AgNO<sub>3</sub> in the final extracts. Overall, we have prepared three N-F co-doped catalysts herein named as TNF1, TNF2, TNF3, and three

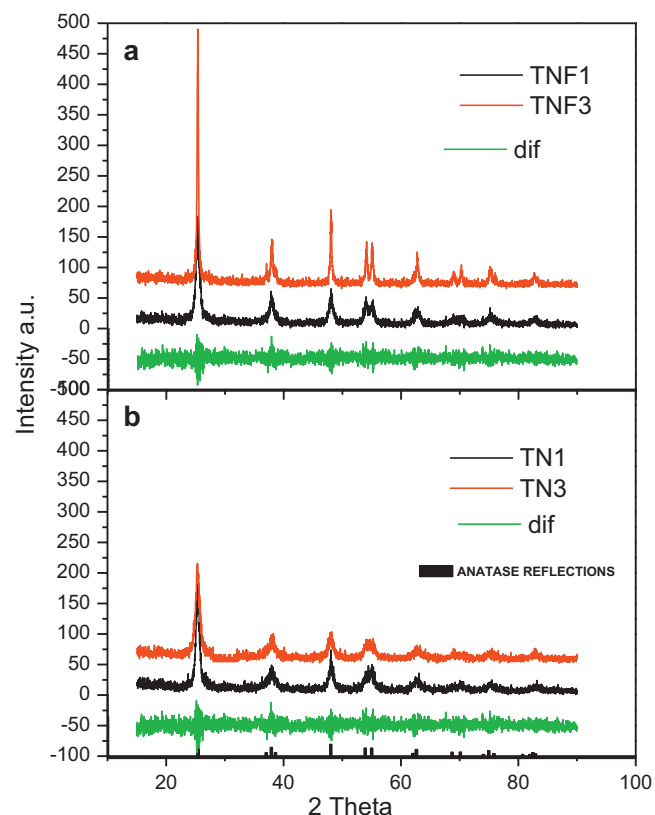


**Fig. 1.** Representative XRD patterns for prepared N-doped and N-F co-doped catalysts. (A) TNF1 sample (black line plot), TNF3 sample (red line plot), difference plot between experimental and theoretical calculated (Rietveld analysis) (green line plot) and reflections of TiO<sub>2</sub> anatase phase according to databank used (column type plot); (B) TN1 sample (black line plot), TN3 sample (red line plot). (For interpretation of the references to color in this figure legend, the reader is referred to the web version of this article.)

N-doped catalysts herein named as TN1, TN2, TN3. The full details of the experimental conditions used for each sample, are listed in Table 1. For comparison, undoped TiO<sub>2</sub> was prepared with the same method.

### 2.2. XRD analysis

The crystal phases of the prepared catalysts were characterized by recording their X-ray diffraction (XRD) patterns using a Bruker Advance D8 instrument employing Cu K radiation ( $\lambda = 1.5418 \text{ \AA}$ ) in the  $2\theta$  range from 10° to 80° with a  $2\theta$  resolution of 0.02°. The XRD patterns were assigned using the Joint Committee on Powder Diffraction Standards (JCPDS) database and then were analyzed with Rietveld refinement using an applicable computer program. Crystal size was calculated by the well known Sheerer's equation:  $d = 0.9\lambda/b \cos \theta$ , where  $d$  is diameter of crystallites in nm,  $\lambda$  the wavelength (nm) of the monochromatic X-ray beam,  $\theta$  is the Bragg angle in degrees, and  $b$  is the FWHM. The results obtained from XRD analysis are presented in Fig. 1 and Table 2.

### 2.3. UV-vis DRS measurements

The ultraviolet-visible diffuse reflectance spectra (UV-vis DRS) of the catalysts were measured by a Perkin-Elmer (Lambda 35) spectrophotometer equipped with an integrating sphere assembly, using BaSO<sub>4</sub> as the reflectance standard, at room temperature, in the wavelength range of 220–800 nm. The UV-vis DRS of the

**Table 1**

The compositions of sols employed for the preparation of all N-doped and N–F co-doped TiO<sub>2</sub> catalysts.

Code name	N:Ti or N/F:Ti molar ratio	NH <sub>4</sub> F (g mol)	NH <sub>4</sub> Cl (g mol)	Tetrabutyl orthotitanate – TBOT (mL mol)	Total sol volume (mL)
TN1	1	–	0.5349–0.01	3.4–0.01	50
TN2	2	–	1.0698–0.02	3.4–0.01	50
TN3	3	–	1.6047–0.03	3.4–0.01	50
TNF1	1	0.3704–0.01	–	3.4–0.01	50
TNF2	2	0.7408–0.02	–	3.4–0.01	50
TNF3	3	1.1112–0.03	–	3.4–0.01	50
Undoped-TiO <sub>2</sub>	–	–	–	3.4–0.01	50

prepared catalysts are shown in Fig. 2(a) while the Kübelka Münk plots are presented in Fig. 2(b).

#### 2.4. EPR experiments

Electron paramagnetic resonance (EPR) spectra were recorded with a Brüker ER200D spectrometer at liquid N<sub>2</sub> temperatures, equipped with an Agilent 5310A frequency counter. Adequate signal to noise ratio was obtained after 5–10 scans. The spectrometer was running under homemade software based on Lab View [25]. Spin quantitation was done using DPPH as spin standard [26]. The effect of light irradiation on EPR spectra of the TiO<sub>2</sub> catalysts was investigated directly irradiating the sample into the EPR cavity using a 450 W (Oriel model 66929) lamp as illumination source equipped with an IR water filter. For the investigation of the O<sub>2</sub><sup>–</sup> radicals formation on the surface of the catalysts under O<sub>2</sub> atmosphere and light conditions, the EPR tube with the TiO<sub>2</sub> catalyst was irradiated at room temperature and ambient O<sub>2</sub> atmosphere for 10 min and then frozen to T=77 K within 5 s.

*Progressive microwave saturation EPR experiments.* The coupling of the N-based paramagnetic species detected in N–F co-doped and N doped catalysts, with the crystal lattice was studied by progressive saturation EPR experiments [27]. The saturation curve is constructed by plotting the EPR signal amplitude (*I*) as a function of the square root of incident microwave power (*P* in Watts) [28]. The saturation data were fitted by the expression  $I(P) = (1 + P/P_{1/2})^{-b/2}$ , where *b* is the inhomogeneity parameter. The adjustable parameter *P*<sub>1/2</sub> is the power at which the signal attains half of its unsaturated value. The comparison of the *P*<sub>1/2</sub> values for a series of TiO<sub>2</sub> samples provides information on the dynamics of the studied paramagnetic centers and their coupling with the solid lattice [27,28] e.g. when we compare systems with the same spin-state and spin-orbit coupling (*g*-tensor), then increased *P*<sub>1/2</sub> values reflect stronger spin-lattice couplings.

*Monitoring of Cr(V)–oxalate intermediates by EPR spectroscopy.* EPR was also used for the detection of Cr(V)–oxalate intermediates formed during the photocatalytic reduction of Cr(VI). The spectra were recorded at 77 K. Typical instrumental conditions were as follows: microwave power, 10 dB, amplifier, modulation amplitude 2 Gpp.

Appropriate volumes of stock solutions of 0.8 mM K<sub>2</sub>Cr<sub>2</sub>O<sub>7</sub> and 4.0 mM oxalic acid were added to previously sonicated 0.1 g L<sup>–1</sup> aqueous TNF1 suspensions, and the pH was adjusted to 1.5 with dilute H<sub>2</sub>SO<sub>4</sub>. The samples were stirred in the dark for 10 min and then irradiated at room temperature into the EPR cavity using the 450 W (Oriel model 66929) lamp as illumination source. At different time intervals the sample was frozen at 77 K within 5 s and the EPR spectrum was recorded.

#### 2.5. Photocatalytic reduction of Cr(VI) in the presence of oxalate

Irradiation experiments were carried out on stirred aqueous solutions using a 200 mL cylindrical pyrex glass UV-reactor equipped with a water-circulating circuit. The irradiation was carried out using a Suntest XLS+ apparatus from Heraeus (Hanau, Germany) equipped with a xenon arc lamp (2200 W) and special glass filters restricting the transmission of wavelengths below 290 nm. An average irradiation intensity of 750 W/m<sup>2</sup> was maintained throughout the experiments. The temperature of samples did not exceed 25 °C using tap-water cooling circuit for the photoreactor. For all photocatalytic runs, a fresh solution (200 mL) containing 0.4 mM K<sub>2</sub>Cr<sub>2</sub>O<sub>7</sub> and 4.0 mM C<sub>2</sub>O<sub>4</sub>H<sub>2</sub> was adjusted to the desired pH with diluted sulfuric acid, and the appropriate catalyst amount was added. Prior to irradiation, suspensions were sonicated for 20 s and magnetically stirred in the dark at 298 K for 30 min to ensure substrate–surface equilibration. The concentration of Cr(VI) after equilibration was taken as the initial concentration (*C*<sub>0</sub>), to discount the adsorption in the dark (which varied between 5% and 7% in the conditions explored in this work) and to evaluate only changes due to irradiation. Samples of 5 mL were periodically withdrawn for quantitative analysis and filtered through 0.45 μm HA Millipore filter. At least duplicated runs were carried out for each condition, averaging the results.

Changes in Cr(VI) concentrations were followed by UV spectroscopy at 349 nm [29]. UV-vis absorption measurements were performed employing a Hitachi U2000 spectrophotometer. Photocatalytic experiments were conducted in air atmosphere, at pH 2 using 1 g L<sup>–1</sup> catalyst concentration for all prepared catalysts. For comparison, undoped TiO<sub>2</sub> prepared with the same method and Degussa-P25 catalysts were evaluated under the same conditions.

**Table 2**

Results of XRD and Rietveld analysis for prepared N doped and N–F co-doped solids.

Code name	XRD Rietveld analysis							<i>E</i> % <sup>a</sup>	<i>R</i> % <sup>a</sup>
	Crystal phase	Space group	<i>a</i>	<i>b</i>	<i>c</i>	FWHM	Crystal size, <i>d</i> (nm)		
TiO <sub>2</sub> databank phase	Anatase TiO <sub>2</sub>	Tetragonal I41	3.784	3.784	9.515	–	–	–	–
TN1	Anatase TiO <sub>2</sub>	Tetragonal I41	3.783	3.783	9.484	0.769	19.0	18.1	22.6
TN2	Anatase TiO <sub>2</sub>	Tetragonal I41	3.783	3.783	9.481	0.974	15.0	18.4	22.8
TN3	Anatase TiO <sub>2</sub>	Tetragonal I41	3.783	3.783	9.476	0.812	18.0	18.8	22.0
TNF1	Anatase TiO <sub>2</sub>	Tetragonal I41	3.788	3.788	9.502	0.827	17.7	18.2	21.8
TNF2	Anatase TiO <sub>2</sub>	Tetragonal I41	3.789	3.789	9.488	0.478	30.6	17.8	21.2
TNF3	Anatase TiO <sub>2</sub>	Tetragonal I41	3.790	3.790	9.485	0.259	56.6	17.4	21.2

<sup>a</sup> Fitting reliability factors, *E*%: profile factor and *R*%: weighted profile factor, are included to show the fitting effectiveness.

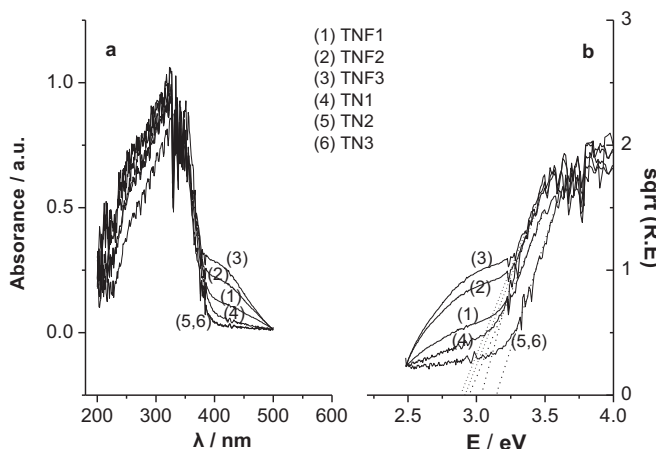


**Fig. 2.** (a) DR UV-vis spectra and (b) Kubelka Münk plots of: undoped all prepared solids. R: absorbance,  $E = 1241.436/\lambda$ : energy in eV,  $\lambda$  = wavelength in nm.

### 3. Results

#### 3.1. XRD characterization

Representative X-ray diffractograms for TN1, TN3, TNF1 and TNF3 solids are shown in Fig. 1. The reflections of  $\text{TiO}_2$  tetragonal anatase phase, space group I41, reported in the databank (JCPDS), are also included in the bottom of Fig. 1 by the bar-diagram. Using the phase obtained for each solid as the starting model, a Rietveld refinement of the obtained XRD data was made based on the methodology developed in Ref. [30]. The bottom-curve of Fig. 1 presents the difference between the experimental and theoretical patterns calculated from the refinement analysis. The refinement parameters including the cell parameters ( $a$ ,  $b$  and  $c$ ), FWHM (observed peak width at half maximum peak height in rad), crystallite size, the reliability factors  $E\%$  (profile factor) and  $R\%$  (weighted profile factor) are presented in Table 2.

The cell parameters (Table 2) for all prepared solids show small differences vs. the theoretical values of pure  $\text{TiO}_2$  anatase phase [31]. This diversification is more pronounced in the N-F co-doped  $\text{TiO}_2$ , showing a more pronounced distortion of the crystal lattice. Crystal lattice distortion is reported to be important for absorption-edge shift toward the visible-light region [31]. In addition, equally important is the diversification of crystallite size values. In the case of N-doped materials, broader XRD patterns were observed, which correspond to low crystallite size values. The crystallite size values for N-F co-doped  $\text{TiO}_2$  solids followed the trend:

$$d_{\text{cryst}, \text{TNF1}} = 17.7 \text{ nm} < d_{\text{cryst}, \text{TNF2}} = 30.6 \text{ nm} < d_{\text{cryst}, \text{TNF3}} = 56.6 \text{ nm}$$

An increment in sharpness of the XRD and a concomitant increment in the crystallite size was observed in the case of N-F co-doped materials.

So, it can be stated that: [i] doping with N ions and co-doping with N and F ions results to final solids with crystal lattice distortion and lower crystal size, [ii] increasing the N/F co-doping ratio increases the crystal size in the final solids.

#### 3.2. UV-vis spectra

The DR UV-vis spectra of the prepared catalysts are presented in Fig. 2(a).

For the doped catalysts, the typical absorption edge due to electronic transitions from valence band to the conduction band of  $\text{TiO}_2$  was modified by the onset of a relatively broad absorption band in the visible region whose intensity depends on the type of

catalyst sample. This band was more intense for N-F/ $\text{TiO}_2$  materials than for N- $\text{TiO}_2$  and decreased progressively in the following order: TNF3 > TNF2 > TNF1.

In the case of N-doped  $\text{TiO}_2$  materials, a weak visible absorption band appeared for TN1 sample. TN2 and TN3 had similar absorbance profiles in the visible region. Band-gap energies,  $E_g$ , for the N-doped and N-F co-doped  $\text{TiO}_2$  photocatalysts were calculated by plotting the transformed Kübelka-Münk function [32a] versus the band gap energy as shown in Fig. 2(b). The calculated  $E_g$  values are listed in Table 4.  $E_g$  values of 3.10 eV were estimated for TN2 and TN3 materials while for the TN1 sample  $E_g$  decreased to 3.01 eV. In the case of N-F co-doped samples,  $E_g$  value decreased with increasing N-F doping i.e. 2.96, 2.91 and 2.81 eV for TNF1, TNF2 and TNF3, respectively. The key-information here is that  $E_g$  values  $\leq 3$  eV correspond to visible light absorption. Thus, doping of  $\text{TiO}_2$  causes the shift of absorption in the visible-light region and this was higher for the N-F co-doped samples (see UV-vis spectra in Fig. 2(a)). The visible-light absorption for N-doped  $\text{TiO}_2$  is associated with the impurity states deriving from N-insertion in the bulk of the titania [15,32b]. Our data show that the concomitant presence of nitrogen and fluorine in the N-F catalysts enhances the visible spectral absorbance with increasing the F-content e.g. the absorbance at 410 nm was 0.147 for TNF1, 0.205 for TNF2, and 0.266 for TNF3, indicating a determinant role of F in promoting N insertion in the  $\text{TiO}_2$  lattice [19,22a].

#### 3.3. EPR characterization of paramagnetic species

The EPR spectra for N doped and N-F co-doped catalysts revealed the presence of N-based paramagnetic species. Typical EPR spectra for TNF1 and TN1 samples in the dark are shown in Fig. 3. The g- and  $^{14}\text{N}$  ( $I=1$ ) hyperfine-tensors for all the paramagnetic species observed by EPR are reported in Table 3. Using these g- and A-tensors, the structural assignment of these centers was performed according to Di Valentin et al. [22]. The values reported by Di Valentin et al. [22] are also included in Table 3 for comparison. The spectra reveal two types of signals denoted as NO centers (type I) and  $\text{N}_b^\bullet$  species (type II) [21,22]. In Fig. 3 the dotted lines mark the g- and  $^{14}\text{N}$ -tensors of the NO and  $\text{N}_b^\bullet$  species.

Di Valentin et al. [21] reported that the NO center is trapped in microvoids of the solid and is detected by EPR when adsorbed on the surface. The more interesting  $\text{N}_b^\bullet$  species (type II) were formed upon calcination of the system after gelification [21,22]. The EPR signal of this  $\text{N}_b^\bullet$  species (Fig. 3), is characterized by an orthorhombic g tensor whose principal values are,  $g_1 = 2.001$ ,  $g_2 = 1.998$ , and  $g_3 = 1.927$  [22].

In Fig. 3(A) and (B) the  $g_2$  (1.998),  $g_3$  (1.927) components of NO species can be resolved with a  $^{14}\text{N}$ -hyperfine splitting at 32.2 G and 9.6 G, respectively. In addition, for TNF1 (Fig. 3(A)) the signal of NO centers with  $g_1 = 2.001$  and a  $^{14}\text{N}$ -hyperfine splitting  $< 1$  G masks the  $g_1$  (2.005) component of  $\text{N}_b^\bullet$  while in TN1 (Fig. 3(B)) both  $g_1$  components of  $\text{N}_b^\bullet$  and NO centers can be resolved at  $g_1(\text{N}_b^\bullet) = 2.005$  and  $g_1(\text{NO}) = 2.001$ , respectively. Light-induced EPR signals of TNF1 and TN1 samples are presented in Fig. 3(C) and (D), respectively. In comparison with dark, upon illumination, the  $\text{N}_b^\bullet$  components were more clearly detectable while the signals of inner  $\text{Ti}^{3+}$  ions ( $g = 1.99$ ,  $g = 1.964$  and  $g = 1.94$ ) appeared in TNF1 (Fig. 3(C)). Finally, in the upper part of Fig. 3(E) and (F) the light-induced signals of TNF1 and TN1 were analyzed under low microwave power. Under these conditions, the  $g_2$  (1.998) component of NO and  $g_3$  (2.003) component of  $\text{N}_b^\bullet$  species were resolved clearly. The  $g = 1.990$  component of lattice  $\text{Ti}^{3+}$  is also clearly detectable in TNF1 (Fig. 3(E)) while in both TNF1, TN1 the decrease of NO signals under lower microwave power is in agreement with previous studies [21,22] reporting that such species are formed in surface microvoids and are unstable. According to

**Table 3**

$g$ - and  $^{14}\text{N}$  ( $I=1$ ) hyperfine-tensors of observed paramagnetic species in N doped and N–F co-doped  $\text{TiO}_2$  prepared with different N and N/F ratios according to Valentim et al. [22] and Berger et al. [35]. With bold font are emphasized the  $g$  contents detected in N doped and N, F co-doped prepared samples.

Paramagnetic species	$g_1$	$g_2$	$g_3$	$A_1/\text{G}$	$A_2/\text{G}$	$A_3/\text{G}$	$g_{  }$	$g_{\perp}$	Code names of solids where paramagnetic species detected
NO	<b>2.001</b>	<b>1.998</b>	<b>1.927</b>	<1	<b>32.2</b>	<b>9.6</b>	—	—	TN1, TN2, TN3, TNF1, TNF2, TNF3
$\text{N}_\text{b}^\bullet$	<b>2.005</b>	2.004	<b>2.003</b>	2.3	4.4	<b>32.3</b>	—	—	TN1, TN2, TN3, TNF1, TNF2, TNF3
$\text{Ti}^{3+}$ lattice	—	—	—	—	—	—	<b>1.99</b>	<b>1.964</b>	TNF1, TNF2, TNF3
$\text{Ti}^{3+}$ surface	—	—	—	—	—	—	<b>1.972</b>	<b>1.954</b>	TN1, TN2, TN3
$\text{O}^{2-}$ [I]	<b>2.0248</b>	<b>2.0096</b>	2.0033	—	—	—	—	—	TN1, TNF1
$\text{O}^{2-}$ [II]	<b>2.0184</b>	<b>2.0096</b>	2.0033	—	—	—	—	—	TN1, TNF1
$\text{O}^-$	—	—	—	—	—	—	2.0046	2.0121	Not detected

[21,22], the N atom of  $\text{N}_\text{b}^\bullet$  species is bound to a lattice-oxygen ion, thus giving rise to paramagnetic species with the unpaired electron in one of the  $\pi^*$  orbitals of the N–O fragment. This electronic configuration results in a  $g_3 = 2.003$  and a quite large  $^{14}\text{N}$ -hyperfine coupling 32.3 G (Fig. 3(E) and (F) and Table 3). The spectrum for the NO-center is manifested with a resolvable feature at  $g_2 = 1.998$  and a  $^{14}\text{N}$ -hyperfine coupling 32.2 G (Fig. 3(E) and (F) and Table 3).

EPR data showed the formation of stable NO and  $\text{N}_\text{b}^\bullet$  centers in the crystal of all N doped and N–F co-doped  $\text{TiO}_2$  samples. In the case of N–F co-doped samples the formation of lattice  $\text{Ti}^{3+}$  ions is favored. These results are in agreement with previous studies [21,22,33]. Li et al. [19,34a] reported that  $\text{F}^-$  ions favor the formation of  $\text{Ti}^{3+}$  ions and oxygen vacancies. In addition, recent EPR studies of F-doped  $\text{TiO}_2$  catalysts [34b,34c] report that presence of fluorine in the lattice induces the formation of reduced  $\text{Ti}^{3+}$  centers that localize the extra electron needed for charge compensation.

Fig. 4(A) and (B) presents EPR spectra of TNF1 and TN1 catalysts measured under illumination at 77 K in order to study the photoresponse of paramagnetic species.

The data in Fig. 4 show light-induced  $\text{N}_\text{b}^\bullet$  and  $\text{Ti}^{3+}$  species in TNF1 sample, while the NO species seem to be less or non-photoactive (Fig. 4(A)). In Fig. 4(B) we can observe the photoresponse of  $\text{N}_\text{b}^\bullet$  species in TN1 sample. Comparing Fig. 4(A) and (B), higher photogeneration is observed for  $\text{N}_\text{b}^\bullet$  species in TNF1 compared to TN1. This fact will be discussed later in combination with the catalytic performance toward Cr(VI) reduction.

Fig. 4(C) and (D) show light minus dark EPR signals e.g. the signals correspond exclusively to photoinduced centers. The following observations can be made: [i] TNF1 had the higher photoinduced signals,  $\text{N}_\text{b}^\bullet$ ,  $\text{Ti}^{3+}$  than all TN samples; [ii] TNF2 showed the same intensities for the photoinduced signals as TN samples; [iii] TNF3 had much lower photoinduced signals than the TN samples; [iv] the intensity of photoinduced signals in the case of N–F co-doped catalysts decreased as the molar ratio of N–F doping increased.

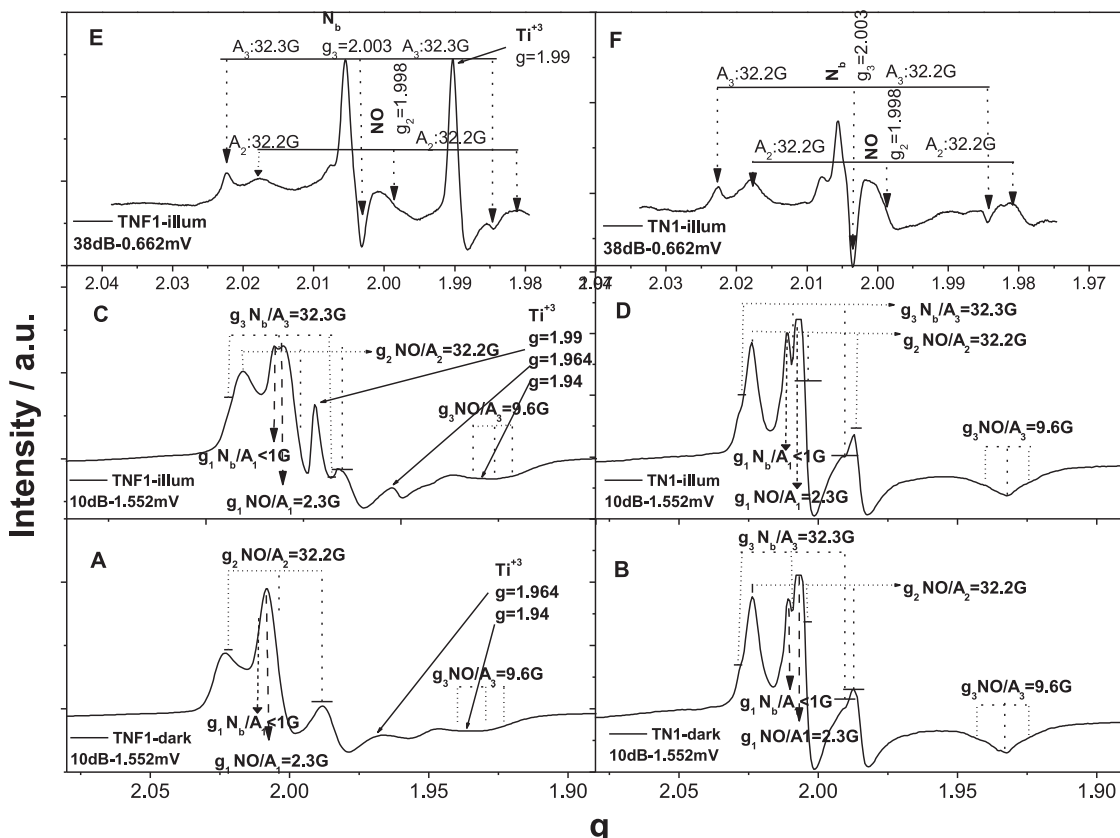
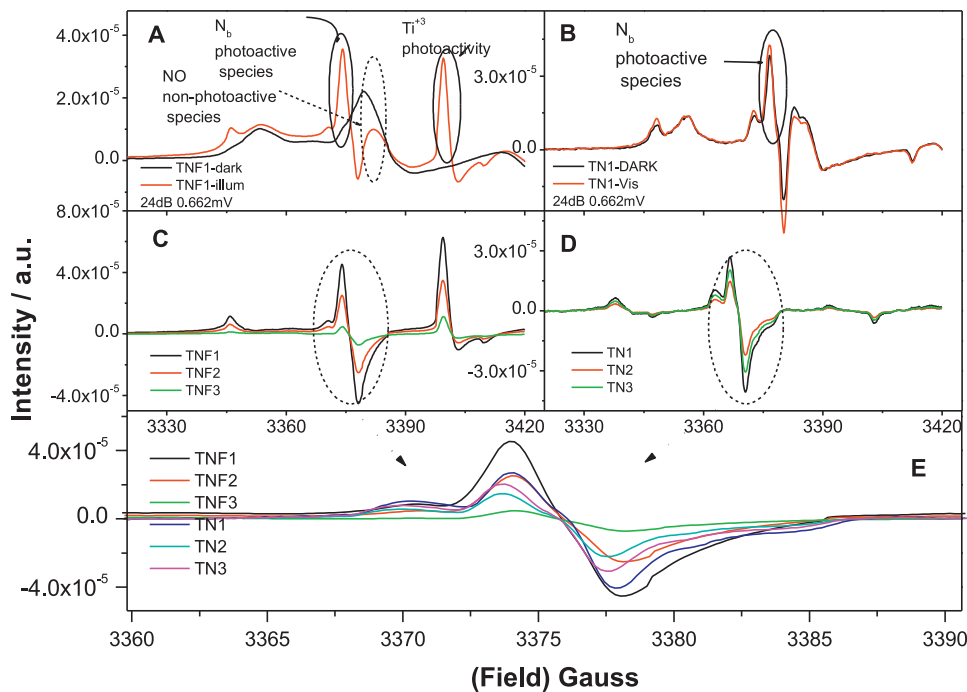


Fig. 3. EPR spectra of the samples with code names TNF1 (A, C and E) and TN1 (B, D and F) at 77 K under dark (A and B) and illumination (C, D, E and F) conditions. Typical experimental condition: (A, B, C and D) amplifier, 1.552 mV; microwave power, 10 dB; sensitivity, 20 mV; time constant, 100 ms; (E and F) amplifier, 0.662 mV; microwave power, 38 dB; sensitivity, 20 mV; time constant, 100 ms.



**Fig. 4.** EPR spectra of the TNF1 (A and C) and TN1 (B and D) catalyst. Measurements carried out at 77 K under illumination. (C) and (D) plots are resulted from the difference of signals in the dark and in the visible light. (For interpretation of the references to color in this figure legend, the reader is referred to the web version of this article.)

Summarizing these results, the signal intensity of N-F co-doped catalysts followed the trend TNF1 > TNF2 > TNF3 ( $N_b^\bullet$  species– $Ti^{3+}$  ions) while in the case of N doped catalysts the trend was TN1 > TN3 > TN2 ( $N_b^\bullet$  species) (Fig. 4(D)).

Based on the intensity of the main peak of the  $N_b^\bullet$  species at  $g_1 = 2.005$  (marked by arrow in Fig. 4), it can be observed that the photo response of  $N_b^\bullet$  species decreased according to the sequence TNF1 > TN1  $\geq$  TNF2 > TN3 > TN2 > TNF3. The same trend was followed for the photocatalytic reduction of Cr(VI) as shown hereafter.

In summary, the EPR data in Figs. 3 and 4 show that the NO centers behave in a different way compared to  $N_b^\bullet$  and  $Ti^{3+}$  centers. It has been reported that NO occupy surface-sites on  $TiO_2$  particles while  $N_b^\bullet$  and  $Ti^{3+}$  is expected to be localized in the bulk of the  $TiO_2$  lattice [21,22]. Our data provide evidence that the behavior of these centers varies among  $TiO_2$  samples of the same doping-family. In order to get further insight into the effect of the  $TiO_2$  crystal lattice on the dynamics of  $N_b^\bullet$  centers we have carried out microwave-power saturation EPR experiments.

*Microwave power saturation study for the  $N_b^\bullet$  centers.* The progressive microwave power saturation data at 77 K for the  $g_1 = 2.005$  signal are displayed in Fig. 5. The signal saturated easily with no changes in the line-shape.

The microwave power saturation values ( $P_{1/2}$ ) for the  $N_b^\bullet$  centers, measured for the various catalysts are listed in Table 4. To better understand the significance of these numbers we briefly reiterate the basic underlying mechanism which results in shifts of the  $P_{1/2}$  values. For  $S = 1/2$  systems, like the ones studied herein for the  $TiO_2$  materials, spin-lattice coupling is the main mechanism which determines the  $P_{1/2}$  values. This spin-lattice coupling is mediated by the g-tensor and the A-tensor [27,28]. Thus, an increase of the  $P_{1/2}$  value for comparable  $S = 1/2$  systems e.g.  $N_b^\bullet$  species in the various N-F catalysts, reflects an enhanced spin-lattice coupling. This can be a result of [i] stronger N–O bonds [ii] positioning of the  $N_b^\bullet$  centers deeper in the crystal. Stronger N–O bond will be manifested as shifts in g-values, which is not the case for our samples (see Table 4). Thus, the higher  $P_{1/2}$  values for the  $N_b^\bullet$  centers can be attributed

to their localization deeper into the crystal sites. More precisely, in the case of N-doped samples the  $P_{1/2}$  values of the  $N_b^\bullet$  centers followed the sequence: TN1 > TN3 > TN2, while the  $P_{1/2}$  sequence for all tested N-F co-doped catalysts is: TNF1 > TNF2 > TNF3.

By combining this information with other chemical/structural information data [20–22] a tighter coupling of the photoactive  $N_b^\bullet$  centers with the lattice of N-F co-doped  $TiO_2$  can be suggested. This could be attributed to deeper localization in the crystal lattice compared to  $N_b^\bullet$  species of N-doped catalysts. Finally, a higher concentration of photoinduced  $N_b^\bullet$  species is observed for N-F co-doped  $TiO_2$ .

*EPR study under  $O_2$ -atmosphere.* In order to investigate the electron scavenging mechanism by surface-adsorbed  $O_2$ , the most efficient samples of N-doped and N-F co-doped catalysts, i.e. TN1 and TNF1, were illuminated under  $O_2$  atmosphere. EPR spectra together with the assignment of the observed signals are shown in (Fig. 6).

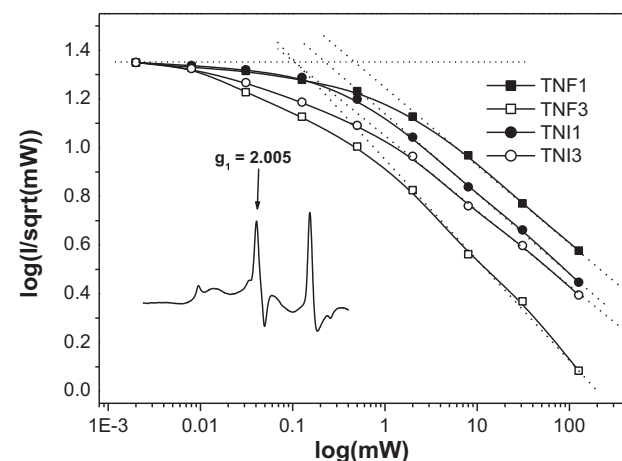


**Fig. 5.** Spin lattice relaxation plots for  $N_b^\bullet$  species at TN1 and TNF1 samples.

**Table 4**

Values of % Cr(VI) reduction at first 15 min irradiation and kinetic constant  $k_1$  for all tested catalysts in Cr(VI) reduction in the presence of oxalate species. In the last column also values of  $P_{1/2}$  for N–F co-doped and N doped samples included.

Catalyst code name	% Cr(VI) reduction after 15 min irradiation	$k_1$ (min <sup>-1</sup> )	$P_{1/2}$ (mW)	$E_g$ (eV)
TNF1_N <sub>2</sub>	44	0.040		
TNF1	44	0.039	0.4775	2.96
TNF2	34	0.023	0.2465	2.91
TNF3	27	0.018	0.2168	2.81
TN1	34	0.024	0.2445	3.01
TN2	29	0.019	0.1956	3.08
TN3	32	0.020	0.2068	3.10
TiO <sub>2</sub> undoped	12	0.011		
P25	34	0.024		

The  $g_{xx}$ ,  $g_{yy}$  and  $g_{zz}$  values of  $O_2^{-\bullet}$  and  $O^{-\bullet}$  radicals are reported in Table 3 based on the study of Berger et al. [35a]. As denoted in Fig. 6, the  $g_{zz}$  components (at 2.0248 and 2.0184) of the two  $O_2^{-\bullet}$  radical types [35a] are resolved in TNF1 and TN1. In addition, the  $g_{yy} = 2.0096$  of both types of  $O_2^{-\bullet}$  is resolved in TNF1. This is also resolved in TN1 although partially overlapped by the strong NO signal.

Under these experimental conditions the  $Ti^{3+}$  lattice ions with  $g$  components 1.99 and 1.96 are clearly detectable in the case of TNF1 sample. In TN1 the  $g = 1.99$  component is too weak, while  $Ti^{3+}$  surface ions can be better resolved as broad components in the region between  $g = 1.98$  and 1.93 according to Barolo et al. [35b].

Thus, the EPR spectra showed that in both TNF1 and TN1 two types of superoxide radicals are trapped under illumination. Based on their intensities of the  $g_{zz}$  signals in Fig. 6, we concluded that higher concentrations of  $O_2^{-\bullet}$  were produced in TN1 compared to TNF1. To summarize, EPR experiments showed that electron capturing by  $O_2$  took place at lower extent in TNF compared to TN catalysts thus, more electrons are available for conducting other

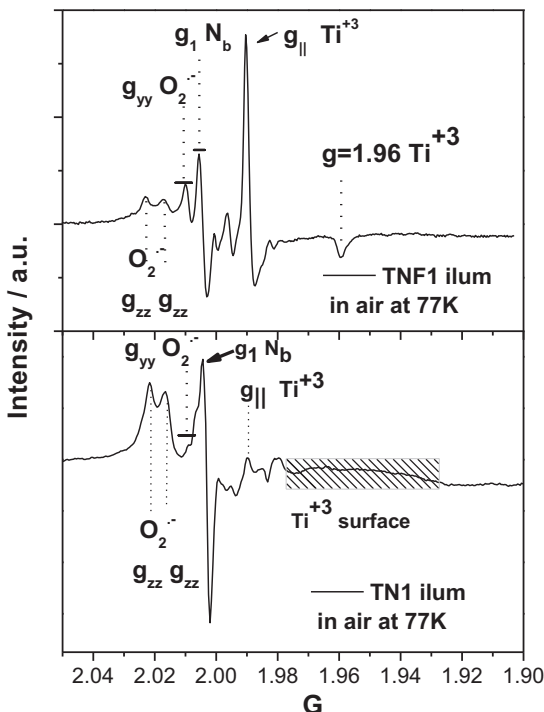


Fig. 6. EPR spectra of TN1 and TNF1 catalysts. Measurements carried out in air at 77 K under illumination. Typical experimental conditions: C.F.: 3420, S.W.: 400, number of steps 512, attenuation 24 dB, modulation 4 Gptp and sensitivity 20 mV.

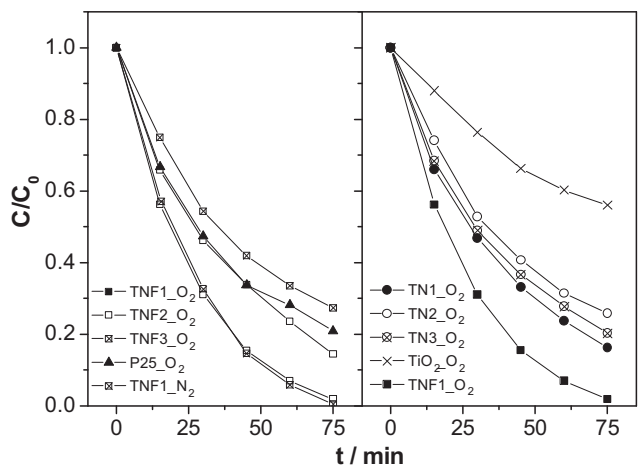


Fig. 7. Time profile of Cr(VI) in the presence of oxalate species reduction of 1 g L<sup>-1</sup> catalyst suspensions at pH 2, under air conditions for all N doped and N–F co-doped prepared catalysts in comparison with undoped TiO<sub>2</sub> sample and Degussa P25. Plot of Cr(VI) reduction for TNF1 catalyst under N<sub>2</sub> condition is also included.

reduction reactions in the presence of appropriate substrates, such as Cr(VI) reduction.

### 3.4. Cr(VI) photoreduction by the TiO<sub>2</sub> catalysts

#### 3.4.1. Kinetic measurements by UV-vis

Fig. 7 shows the time-profiles of Cr(VI) reduction, at pH 2 by the N doped and N–F co-doped TiO<sub>2</sub> catalysts. Excess of oxalate ions was used since it has been largely demonstrated that addition of organic donors able to chelate the TiO<sub>2</sub> surface accelerates the reduction of Cr(VI) in photocatalytic systems, the synergy being very dependent on the nature of the reducing agent [36].

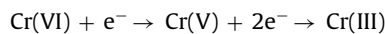
From Fig. 7 the first-order kinetic constants  $k$  (min<sup>-1</sup>) and the % of Cr(VI) reduction after 15 min of irradiation, were derived for all tested catalysts (Table 4). Accordingly, the photocatalytic activity followed the sequence: TNF1 > TN1 > TNF2  $\cong$  P25 > TN3 > TN2 > TNF3 > undoped-TiO<sub>2</sub>.

The kinetics (Fig. 7 and Table 3) showed a much higher photocatalytic activity for all N doped and N–F co-doped catalysts vs. undoped TiO<sub>2</sub>. In addition, the TNF1 and TN1 samples had higher catalytic activity than Degussa-P25 catalyst.

#### 3.4.2. EPR studies

According to previous studies in homogeneous systems, oxidation of oxalic acid by Cr(VI) involves formation of Cr(V)–oxalate complexes as intermediates [36–42]. In agreement with these results, in the present work, Cr(V) species were also detected in the heterogeneous TNF1/Cr(VI)/oxalate system by EPR. Fig. 8(inset) shows an EPR spectrum recorded at 298 K, under continuous UV-irradiation of a sample containing 0.1 g L<sup>-1</sup> TNF1, 4.0 mM oxalic acid, and 0.8 mM K<sub>2</sub>Cr<sub>2</sub>O<sub>7</sub>, pH 1.5. The axial signal with  $g_{1,2} = 1.97$  and  $g_3 = 1.971$  is assigned to Cr(V)–oxalate [37]. Using this EPR signature, Fig. 8 shows the time-dependence of the Cr(V)–oxalate complexes as a function of irradiation time.

A bell-shaped curve is obtained, Fig. 8, which consist of a rapid initial Cr(V)–oxalate formation in agreement with previous studies [37,40,41], followed by a plateau for about 45 min, a time period for completing more than 80% of Cr(VI) reduction (Fig. 7), then followed by a rapid decrease of Cr(V)–oxalate concentration. In accordance with previous reports [37,40–42] such bell-shaped curve can be attributed to sequential one-electron-transfer reactions.



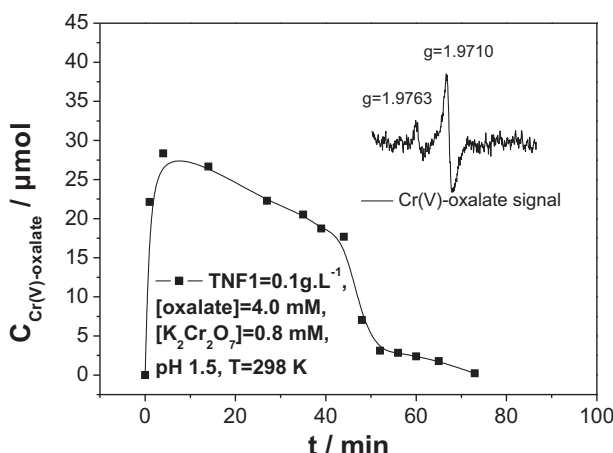


**Fig. 8.** Time dependence of Cr(V)-oxalate intermediates involved in the Cr(VI) reduction obtained under continuous irradiation in EPR spectra. Conditions:  $[C_2O_4H_2] = 4.0\text{ mM}$ ,  $[K_2Cr_2O_7] = 0.8\text{ mM}$ , pH 1.5,  $T = 298\text{ K}$ . Inset figure: EPR spectra of the Cr(V) intermediates formed under continuous irradiation of a TNF1 suspension ( $0.1\text{ g L}^{-1}$ ) at pH 1.5. Conditions: central field  $3498\text{ G}$ , modulation amplitude  $1.25\text{ Gpp}$ .

#### 4. Discussion

The EPR analysis has revealed several key-characteristics for the prepared  $\text{TiO}_2$  catalysts: [i] both N doped and N-F co-doped catalysts bear characteristic N-based paramagnetic centers; they contained weakly physisorbed molecular NO species which were non-photoactive as well as bulk  $\text{Nb}^\bullet$  species which showed high photoactivity; [ii] more  $\text{Ti}^{3+}$  species located inside the lattice of  $\text{TiO}_2$  were detected in N-F co-doped materials because of the presence of  $\text{F}^-$  ions which create oxygen vacancies [19,21,34], while in N-doped materials surface  $\text{Ti}^{3+}$  ions were detected (see Fig. 6); [iii] surface-adsorbed  $\text{O}_2^{\bullet-}$  radicals were detected in both N, F co-doped and N doped solids but in higher quantities for the latter catalysts.

Di Valentin et al. have extensively studied the photocatalytic response of N doped [21] and N-F co-doped  $\text{TiO}_2$  [22] materials. Based on theoretical calculations for N-F  $\text{TiO}_2$  catalysts they suggested that the formation of  $\text{Nb}^\bullet$  species increases the valence band energy  $E_{VB}$  level while the formation of  $\text{Ti}^{3+}$  species results also in the decrease of conduction band energy  $E_{CB}$  level as shown in Fig. 9(a).

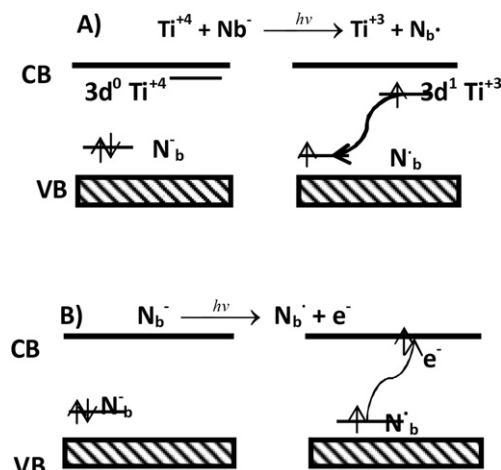


**Fig. 9.** Electronic band structure modifications resulting from the interactions between: (A)  $\text{Nb}^\bullet$  and  $\text{Ti}^{3+}$  (oxygen vacancy) defects at N-F co-doped prepared materials and (B)  $\text{Nb}^\bullet$  species at N doped prepared materials.

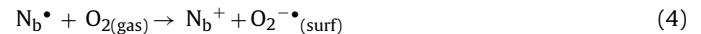
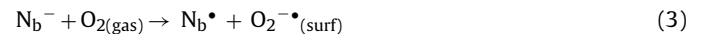
An electron transfer occurs between  $\text{Nb}^\bullet$  species and  $\text{Ti}^{3+}$  (Fig. 9(a)) which are localized inside the lattice, according to the Eq. (1):



In addition, in the case of N-doped  $\text{TiO}_2$  solids, where lattice  $\text{Ti}^{3+}$  centers were not detected, electron transfer takes place under irradiation via the transformation of diamagnetic  $\text{Nb}^\bullet$  species to paramagnetic  $\text{Nb}^\bullet$  (Fig. 9(b)) according to the following route:



Besides, as shown in Fig. 6 and in accordance with previous reports [22,34], in the presence of oxygen in the reaction medium a fraction of photoexcited electrons is scavenged by  $\text{O}_2$ , producing adsorbed  $\text{O}_2^{\bullet-}$  through the route:



Furthermore, recent reports [34b,35b] have shown that a possible route for the formation of  $\text{O}_2^{\bullet-}$  radical could be through the oxidation of  $\text{Ti}^{3+}$  ions:



The photocatalytic routes described by Eqs. (1) and (2) are in accordance with the  $E_g$  values listed in Table 4. N-F co-doped  $\text{TiO}_2$  samples have lower  $E_g$  values, i.e.  $2.81\text{--}2.96\text{ eV}$ , while N-doped samples have  $E_g = 3.01\text{--}3.10\text{ eV}$ . The lower  $E_g$  of N-F compared to N doped  $\text{TiO}_2$  are also in agreement with the observation that  $\text{Nb}^\bullet$  species are more photoactive in TNF1 than TN1 sample (Fig. 4(A) and (B)). Thus, if the photocatalytic efficiency was determined only by the  $E_g$  values, all N-F co-doped catalysts should exhibit higher catalytic activity than all N doped catalysts which was not the case. Despite this, the concentrations of formatted  $\text{Nb}^\bullet$  species seem to play a key-role in the reduction ability of the catalysts. Therefore as mentioned above, the trend in  $\text{Nb}^\bullet$  concentration (see Fig. 4(E)) is in full agreement with the trend in catalytic Cr(VI) reduction.

The formation of  $\text{Nb}^\bullet$  species depends also on the crystallinity of the catalysts. In Table 2 we noticed that the crystallite size for the N-F co-doped catalysts correlates with the N-F doping molar ratio. In N-F co-doped catalysts the concentration of  $\text{Nb}^\bullet$  species decreases as the crystallite size increases. So, the highest photo-generated  $\text{Nb}^\bullet$  species and the highest Cr(VI)-reduction ability was detected for the TNF1 catalyst, which has the lowest crystallite size. On the other hand, in TNF3, the catalyst with the highest crystallite size, the lowest concentration of  $\text{Nb}^\bullet$  species was detected and the lowest Cr(VI)-reduction ability among all tested catalysts. It must be also noticed that TNF3 had the lowest  $E_g$  value =  $2.82\text{ eV}$ . Despite this fact, TNF3 presented the lowest catalytic activity because of the limited formation of  $\text{Nb}^\bullet$  species caused by the increase of crystallite size. All N-doped catalysts had quite similar crystallite size. Small variations in crystallite size are correlated with small variations in concentration of  $\text{Nb}^\bullet$  species (see Fig. 4(D)) that explains the smaller differentiation among the catalytic activity of N-doped catalyst compared to N-F co-doped catalysts (see Fig. 7).

Concerning the electron capture mechanism by surface  $\text{O}_2$ , we postulate the following explanation for the observed data: for the TNF catalysts, the electrons in energy states below the CB of  $\text{TiO}_2$  have weaker reduction ability, so they can reduce preferably strong oxidation agents such as Cr(VI). Thus,  $\text{O}_2$  cannot compete efficiently with Cr(VI) for the photogenerated electrons, although electron capturing by  $\text{O}_2$  is feasible, as shown in Fig. 6. The above consideration was confirmed by studying the reduction of Cr(VI) by TNF1 catalyst under air-equilibrated and  $\text{N}_2$ -purged suspensions that exhibited almost identical reaction rates (Fig. 7 and Table 4).

This is beneficial for the activity of the N–F  $\text{TiO}_2$  toward reductive processes such as Cr(VI) reduction. On the contrary, for the TN catalysts  $\text{O}_2$  can compete more efficiently with Cr(VI) for the photogenerated electrons as observed by the higher intensity of  $\text{O}_2^{\cdot-}$  signals (Fig. 6).

Overall, the present data show that the Cr(VI)-reduction ability of the N and N–F co-doped  $\text{TiO}_2$  catalysts seems to be a quite perplexing process which incorporates several factors. Some of them that were probed herein are: [i] the quantity of the photogenerated  $\text{Nb}^{\bullet}$  is related to the site where  $\text{Nb}^{\bullet}$  species are formed (surface or lattice); [ii] the crystallite size; [iii] the position of energy states below the conduction band that is related to the ability of electron transfer in Cr(VI) or  $\text{O}_2$ . The optimized catalyst having the appropriate characteristics of the above-mentioned factors is TNF1 which exhibited a high efficiency for the photocatalytic reduction of Cr(VI).

## 5. Conclusions

N doped and N–F co-doped  $\text{TiO}_2$  catalysts were prepared via a sol–gel method. Anatase phase with tetragonal I41 space-group was formed in all cases. Both N-doping and N–F co-doping caused distortion of  $\text{TiO}_2$  crystal lattice and exhibited a shift of the absorption edge of the photocatalysts toward visible wavelengths. All N and N–F doped  $\text{TiO}_2$  catalysts were efficient catalysts for the reduction of Cr(VI) in the presence of oxalate ions. The catalytic yield was superior to the undoped  $\text{TiO}_2$  while TNF1 and TN1 catalysts showed higher activity than the Degussa-P25  $\text{TiO}_2$  catalyst.

The following characteristics were observed for N–F co-doped and N doped  $\text{TiO}_2$  catalysts: (i) lower  $E_g$  and subsequently higher absorption at visible wavelengths was obtained for the N–F co-doped catalysts compared to N-doped ones, and with the increment of N–F dosage; (ii) F ions favor formation of lattice  $\text{Ti}^{3+}$  in N–F co-doped solids which leads to lower energy-cost electron transfer route ( $\text{Ti}^{4+} + \text{Nb}^{\bullet-} \rightarrow \text{Ti}^{3+} + \text{Nb}^{\bullet}$ ) while the  $\text{Nb}^{\bullet-} \rightarrow \text{Nb}^{\bullet} + \text{e}^-$  route is adopted in N-doped solids; (iii) F ions have a double effect; they favor the incorporation of  $\text{Nb}^{\bullet}$  photogenerated species deeper into the crystal lattice. However, the increment of F concentration increases crystal-size which in turn causes a decrease in quantity of  $\text{Nb}^{\bullet}$  species; (iv) for the TNF catalysts, the electrons in states below the CB of  $\text{TiO}_2$  can reduce preferably Cr(VI), while  $\text{O}_2$  can compete efficiently with Cr(VI) for the photogenerated electrons in the case of TN catalysts.

## Acknowledgements

This research has been co-financed by the European Union (European Social Fund – ESF) and Greek national funds through the Operational Program “Education and Lifelong Learning” of the National Strategic Reference Framework (NSRF) – Research Funding Program: THALIS. Investing in knowledge society through the European Social Fund.

## References

- [1] M. Kitano, M. Matsuoka, M. Ueshima, M. Anpo, *Applied Catalysis A: General* 325 (2007) 1–14.
- [2] A. Fujishima, T.N. Rao, D.A. Tryk, *Journal of Photochemistry and Photobiology C: Photochemistry Review* 1 (2000) 1–21.
- [3] K.T. Ranjit, B. Viswanathan, *Journal of Photochemistry and Photobiology A: Chemistry* 108 (1997) 79–84.
- [4] L.Q. Jing, X.J. Sun, B.F. Xin, B.Q. Wang, W.M. Cai, H.G. Fu, *Journal of Solid State Chemistry* 177 (2004) 3375–3382.
- [5] Z.L. Liu, B. Guo, L. Hong, H.X. Jiang, *Journal of Physics and Chemistry of Solids* 66 (2005) 161–167.
- [6] A.W. Xu, Y. Gao, H.Q. Liu, *Journal of Catalysis* 207 (2002) 151–157.
- [7] C. Burda, Y.B. Lou, X.B. Chen, C.S. Samia, J. Stout, J.L. Gole, *Nano Letters* 3 (8) (2003) 1049–1051.
- [8] Y. Choi, T. Umebayashi, M. Yoshikawa, *Journal of Materials Science* 39 (2004) 1837–1839.
- [9] T. Ohno, M. Akiyoshi, T. Umebayashi, K. Asai, T. MitSui, M. Matsumura, *Applied Catalysis A: General* 265 (2004) 115–121.
- [10] X. Hong, Z. Wang, W. Cai, F. Lu, J. Zhang, Y. Yang, N. Ma, Y. Liu, *Chemistry of Materials* 1 (2005) 1548–1552.
- [11] J. Xu, Y. Ao, D. Fu, C. Yuan, *Applied Surface Science* 254 (2008) 3033–3038.
- [12] L. Zhou, J. Deng, Y. Zhao, W. Liu, L. An, F. Chen, *Materials Chemistry and Physics* 117 (2009) 522–527.
- [13] X. Li, R. Xiong, G. Wei, *Catalysis Letters* 125 (2008) 104–109.
- [14] M. Pelaez, A.A. de la Cruz, E. Stathatos, P. Falaras, D.D. Dionysiou, *Catalysis Today* 144 (2009) 19–25.
- [15] D. Li, H. Haneda, S. Hishita, N. Ohashi, *Chemistry of Materials* 17 (2005) 2588–2595.
- [16] D.-G. Huang, S.-J. Liao, J.-M. Liu, Z. Dang, L. Petrik, *Journal of Photochemistry and Photobiology A: Chemistry* 184 (2006) 282–288.
- [17] A.K. Rumaiz, J.C. Woicik, E. Cockayne, H.Y. Lin, G.H. Jaffari, *Applied Physics Letters* 95 (2009) 262111–262114.
- [18] Z. Zhang, J. Long, X. Xie, H. Zhuang, Y. Zhou, H. Lin, R. Yuan, W. Dai, Z. Ding, X. Wang, X. Fu, *Applied Catalysis A: General* 425–426 (2012) 117–124.
- [19] D. Li, N. Ohashi, S. Hishita, T. Kolodiazhnyi, H. Haneda, *Journal of Solid State Chemistry* 178 (2005) 3293–3302.
- [20] (a) Q. Wang, C. Chen, W. Ma, H. Zhu, J. Zhao, *Chemistry – A European Journal* 15 (2009) 4765–4769;  
 (b) A. Kleiman, A. Marquez, M.I. Vera, J.M. Meichtry, M.I. Litter, *Applied Catalysis B: Environmental* 101 (3–4) (2011) 676–681;  
 (c) S.K. Choi, H.S. Yang, J.H. Kim, H. Park, *Applied Catalysis B: Environmental* 121–122 (2012) 206–213.
- [21] C. Di Valentin, E. Finazzi, G. Pacchioni, A. Selloni, S. Livraghi, M.C. Paganini, E. Giannello, *Chemical Physics* 339 (2007) 44–56.
- [22] (a) C. Di Valentin, E. Finazzi, G. Pacchioni, *Chemistry of Materials* 20 (2008) 3706–3714;  
 (b) S. Livraghi, M.C. Paganini, E. Giannello, A. Selloni, C. Di Valentin, G. Pacchioni, *Journal of the American Chemical Society* 128 (2006) 15666–15671;  
 (c) M. Chiesa, E. Giannello, M. Che, *Chemical Reviews* 110 (2010) 1320–1347.
- [23] Y. Xie, X. Zhao, Y. Li, Q. Zhao, X. Zhou, Q. Yuan, *Journal of Solid State Chemistry* 181 (2008) 1936–1942.
- [24] M.L. Ojeda, M. Bizarro, A. Campero, *Journal of Sol–Gel Science and Technology* 60 (2011) 108–115.
- [25] G. Grigoropoulou, K.C. Christoforidis, M. Louloudi, Y. Deligiannakis, *Langmuir* 23 (2007) 10407–10418.
- [26] K.C. Christoforidis, M. Louloudi, E.R. Milaeva, Y. Sanakis, Y. Deligiannakis, *Molecular Physics* 105 (2007) 2185–2194.
- [27] Y. Deligiannakis, C. Jegerschld, A.W. Rutherford, *Chemical Physics Letters* 270 (1997) 564–572.
- [28] (a) J.R. Harbridge, S.S. Eaton, G.R. Eaton, *Journal of Physical Chemistry A* 107 (2003) 598–610;  
 (b) S.S. Eaton, *Coordination Chemistry Reviews* 83 (1988) 29–72.
- [29] C. Wei, S. German, S.R. Basak, K. Rajeshwar, *Journal of the Electrochemical Society* 140 (1993) 829–834, L60–L62.
- [30] H.M. Rietveld, *Acta Crystallographica* 22 (1967) 151–152.
- [31] Y. Xie, Y. Li, X. Zhao, *Journal of Molecular Catalysis A: Chemical* 277 (2007) 119–126.
- [32] (a) P. Xu, L. Mi, P.N. Wang, *Journal of Crystal Growth* 289 (2006) 433–439;  
 (b) D.-G. Huang, S.-J. Liao, J.-M. Liu, Z. Dang, L. Petrik, *Journal of Photochemistry and Photobiology A: Chemistry* 184 (2006) 282–288.
- [33] S. Livraghi, A. Votta, M.C. Paganini, E. Giannello, *Chemical Communications* 4 (2005) 498–500.
- [34] (a) J. Xu, Y. Ao, D. Fu, C. Yuan, *Applied Surface Science* 254 (2008) 3033–3038;  
 (b) J.C. Yu, J. Yu, W. Ho, Z. Jiang, L. Zhang, *Chemistry of Materials* 14 (2002) 3808–3816;  
 A.M. Czoska, S. Livraghi, M. Chiesa, E. Giannello, S. Agnoli, G. Granozzi, E. Finazzi, *Journal of Physical Chemistry C* 112 (2008) 8951–8956;
- [35] (a) T. Berger, M. Sterrer, O. Diwald, E. Knozinger, D. Panayotov, T.L. Thompson, J.T. Yates Jr., *Journal of Physical Chemistry B* 109 (2005) 6061–6068;  
 (b) G. Barolo, S. Livraghi, M. Chiesa, M.C. Paganini, Elio Giannello, *Journal of Physical Chemistry C* 116 (2012) 20887–20894.
- [36] B. Deng, A.T. Stone, *Environmental Science and Technology* 30 (1996) 463–472.
- [37] J.J. Testa, M.A. Grela, M.I. Litter, *Environmental Science and Technology* 38 (2004) 1589–1594.
- [38] R.F. Howe, M. Gratzel, *Journal of Physical Chemistry* 91 (1987) 3906–3909.
- [39] R.P. Farrell, R.J. Hudd, P.A. Lay, R. Bramley, S. Brumby, J.-Y. Ji, *Inorganic Chemistry* 28 (1989) 3401–3403.
- [40] J. Srinivasan, J. Rocek, *Journal of the American Chemical Society* 96 (1974) 127–133.
- [41] F. Hasan, J. Rocek, *Journal of the American Chemical Society* 94 (1972) 9073–9081.
- [42] S. Signorella, M. Rizzotto, M. Mulero, S. Garcia, M. Frascaloli, L.F. Sala, *Journal of Chemical Education* 69 (7) (1992) 578–580.